A Validation Procedure for a Polarimetric Weather Radar Signal Simulator

Elisa Barcaroli, Alberto Lupidi, Luca Facheris, Fabrizio Cuccoli, *Member, IEEE*, Haonan Chen, and Chandrasekar V. Chandra, *Fellow, IEEE*

***Abstract*— A simulator of weather radar signals can be exploited as a useful reference for many applications, such as weather forecasting and nowcasting models or for training artificial intelligence systems designed to optimize the trajectory of aircrafts with the purpose to reduce flight hazard and fuel consumption. However, before being used, it must be accurately examined under different operating conditions, in order to evaluate the consistency of the outputs produced. In this paper, we present a validation procedure for a newly developed polarimetric weather radar simulator (POWERS). The goal is to assess the ability of the simulator to deal with any kind of input data, be they simulated and real raindrop-size distributions, or outputs generated by numerical weather prediction models. Three different approaches are proposed, each providing a connection between meteorological inputs and the radar observables simulated by POWERS. The analysis is carried out in the case of rainfall, both at S- and X-bands.**

***Index Terms*— Doppler radar, meteorological radar, radar polarimetry, radar signal processing, simulation software, T-matrix.**

I. Introduction

METEOROLOGICAL radars are currently the fundamental tools for weather monitoring and forecasting. Radar measurements of weather targets, in addition to providing quantitative measurements of precipitation with high resolution both in time and space, also improve the awareness about severe storms and the quality of the prediction models through data assimilation [1], [2]. Moreover, by exploiting the Doppler effect and the full polarization vector information, it is possible to estimate not only the intensity of the phenomenon but also its nature, composition, and velocities of its components. Indeed, when the target polarimetric characteristics along with Doppler features can be retrieved with sufficient accuracy, polarimetric radars allow better precipitation measurements, classification of hydrometeors, accurate hazard assessment, and better correction of attenuation due to propagation [3]. Recent studies evidenced the importance of radar polarimetry also in the avionic field, where dual polarization could increase the awareness about the actual presence of severe storms, giving pilots an important support to take the best decision in terms of flight safety [4].

A realistic numerical simulation can provide a controlled environment for a large variety of purposes. For instance, extreme weather scenarios can be simulated to test the robustness and limitations of signal processing techniques, which help to identify and scrutinize factors that may have been overlooked during the development process [5]. In order to examine the advantages that polarimetry could bring to future avionic weather radar systems, Lischi *et al.* [6], [7] developed a radar simulator called polarimetric weather radar simulator (POWERS).

The POWERS architecture was conceived to blend flexibility and computational efficiency with a high level of adherence to both the physics of the weather phenomenon and the signal acquisition process of a real radar system. This need derived from the fact that it had to train and test the processing algorithms aimed at improving the real-time weather awareness on board. Such algorithms were then implemented on an electronic flight bag (EFB) acting as a decision support system to help pilots to trace alternative routes, avoiding dangerous weather events. The POWERS products have been used to feed the EFB on flight simulators (AIRBUS 320 and ATR72, see [8]) for testing the benefits of polarimetric weather radars in realistic operative flight conditions. For this reason, a statistical approach was adopted combined with a microphysical modeling of precipitation. Indeed, while there exist—as evidenced in the following—more physically accurate simulators, such an approach reduces significantly the computational burden and the related processing time.

Several simulators are illustrated in the literature that can generate directly the weather radar moments or the time series from which the radar moments can be derived. According to the classification proposed by Byrd *et al.* [9], the time

Manuscript received April 16, 2018; revised July 9, 2018; accepted August 23, 2018. Date of publication September 27, 2018; date of current version December 24, 2018. This work was supported by the European Union's Seventh Framework Program (FP7/2007-2013) for the Clean Sky Joint Technology Initiative under grant agreements no. 619236 (X-WALD). The work of H. Chen and Chandrasekar V. Chandra was supported by the National Science Foundation Hazards Science, Engineering, and Education for Sustainability Program. The work of Chandrasekar V. Chandra was supported by the NASA GPM/PMM Project. The work of H. Chen was supported by the NOAA/Earth System Research Laboratory under NRC Research Associateship Award. *(Corresponding author: Luca Facheris.)*

E. Barcaroli, A. Lupidi, and F. Cuccoli are with the CNIT—Radar and Surveillance Systems Laboratory, 56124 Pisa, Italy (e-mail: elisa.barcaroli@for.unipi.it; alberto.lupidi@cnit.it; fabrizio.cuccoli@cnit.it).

L. Facheris is with the Department of Information Engineering, University of Florence, 50139 Florence, Italy (e-mail: luca.facheris@unifi.it).

H. Chen is with the Physical Sciences Division of NOAA—Earth System Research Laboratory, Boulder, CO 80305-3337 USA, and also with the Colorado State University, Fort Collins, CO 80523 USA (e-mail: haonan.chen@colostate.edu).

C. V. Chandra is with the Department of Electrical and Computer Engineering, Colorado State University, Colorado, Fort Collins, CO 80523 USA (e-mail: chandra@engr.colostate.edu).

Color versions of one or more of the figures in this paper are available online at http://ieeexplore.ieee.org.

Digital Object Identifier 10.1109/TGRS.2018.2868144

series simulators can be differentiated by the way they populate, through different "scattering centers" (SCs), the radar resolution volume (RRV). They define two macro groups of SCs, according to what each SC represents for the simulator: homogeneous SCs (HSCs) and bulk SCs (BSCs). The first group includes all the simulators that consider each SC as representative of a group of hydrometeors, characterized by uniformity of diameter, shape, and orientation. This group allows to precisely control the drop-size distribution (DSD) model utilized. On the contrary, for the second group of simulators, the SC represents a group of hydrometeors that follow some heterogeneous distribution of diameter, shape, and orientation. In HSCs simulators, randomness is guaranteed by the variety of the microphysical characteristics associated with the simulated hydrometeors. However, an extremely large number of SCs are necessary to reach an adequate number of elements as needed to properly reproduce a given DSD. This typically implies that there are limitations in the generation of the time series within a single-resolution radar cell [10], [11]. In BSCs simulators, randomness is reached by combining the radar measurables obtained from each RRV, with a given weatherlike radar signal model [5], [9], [12].

Time series simulators had a long evolution: from the pioneering work by Zrnić [13] that was able to reproduce a single weatherlike spectrum of any desired shape, to the latest BSC methods combined with numerical weather prediction (NWP) models that produce 3-D simulations. Notable those by Capsoni *et al.* [10], May *et al.* [12], or Cheong *et al.* [5] that implemented a BSC simulator capable of generating realistic 3-D radar time series data, whose characteristics were directly derived from a high-resolution numerical weather model (Advanced Regional Prediction System).

In this context, Lischi [7] and Lupidi *et al.* [14] proposed in 2016 a newer version of POWERS that merges the BSC approach with the advantages offered by the NWP model called weather research and forecast (WRF) [15]. The uniqueness of POWERS is therefore that it takes into account both the statistical properties of radar signals and the microphysical constraints. On the one hand, the computational cost is significantly reduced compared to the purely physical-based method. On the other hand, POWERS considers the particle size distribution information to ensure the microphysical properties of precipitation. It is also worth noting that as shown by Jung *et al.* [17], polarimetric radar data simulators (such as POWERS) that are based on two-moment or higher moment microphysics schemes can also be profitably exploited to evaluate the performance of NWP models.

The objective of this paper is to establish a validation procedure for this innovative simulator and demonstrate the consistency between the simulated data/signals and the real observations. Some authors have analyzed the outputs of NWP-based simulators [11], [18], [19]. Typically, they check the self-consistency of the simulated signals by examining whether the polarimetric parameters fall within a reasonable/expected range, for a given kind of precipitation, or by qualitatively evaluating their similarity with respect to the radar observations. However, strict rules or index parameters to quantitatively determine the consistency of the data produced have not been provided so far.

In this paper, we present a validation approach to assess the ability of an NWP-based simulator to respond to heterogeneous scenarios. From a theoretical point of view, the approach described herein can be applied to any kind of NWP-based simulator, but for its practical use in this paper, it has been suited to the POWERS features. The procedure consists of three validation checks, corresponding to progressively increasing levels of complexity of the input to the simulator and aimed at assessing its ability to respond to them. At the first level, a synthetic scenario characterized by constant DSD and meteorological parameters is forced as input, and the basic functions required by a weather radar simulator are checked. At the second level, the behavior of the simulator is checked when it is fed by real data. Finally, at the third level, the check is made when the simulator works in a fully stand-alone mode, without forcing any kind of input. This approach has not only assessed the features of the simulator in terms of flexibility and consistency with respect to variable inputs but also allowed us to identify potential simulation issues.

This paper is structured as follows. In Section II, we provide a brief overview of the simulator so that the validation procedure can be better clarified together with the weaknesses and strengths of the simulator itself. In the following sections, we discuss the three aforementioned validation checks. Section III, thus, describes the first one, where a simplified DSD model is used and all the microphysical parameters necessary to create the synthetic weather volume are set constant. The main effort here was to find an independent physically based relation useful to choose the POWERS meteorological inputs in an organized way. Section IV deals with the second validation check where a controlled environment is generated as in the previous check level, with the difference that in this case the simulator is fed with real DSD data acquired during a measurement campaign. Finally, Section V describes the third and last check where the validation is carried out in a heterogeneous scenario that is independently and fully provided by WRF as input to the simulator.

We point out that POWERS is capable of producing radar echoes coming from different hydrometeors classes such as rain, graupel, hail, and snow aggregates. However, the radar signature of rainfall is the most known for all frequencies and a large database is available for testing real data. For this main reason (and others that will be recalled in the conclusion), the validation procedure proposed herein focuses on this class. The simulations were carried out both at S- and X-bands and the contribution by cloud liquid water has not been accounted for since its effects are negligible at those bands.

II. Simulator Overview

A. Simulator

In this paper, the WRF model has been selected to generate the weather scenario where POWERS operates. This weather scenario constitutes the "truth" reference, based on which POWERS generates the in-phase and quadrature (I and Q) signals time series that would be observed at the output of the receiver of a fully polarimetric weather radar and from which the weather radar observables are finally obtained. This allows

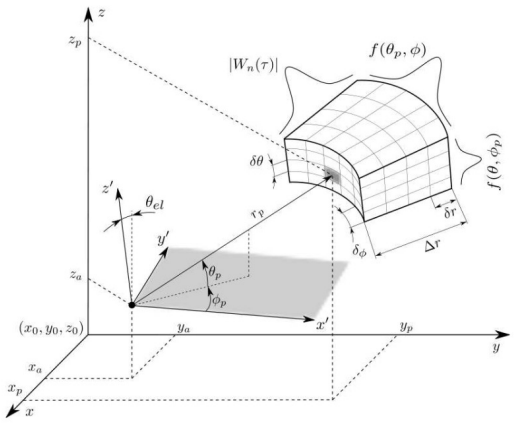

Fig. 1. Radar system geometry and RRV segmentation implemented in the simulator POWERS.

one to evaluate each element of the processing chain (e.g., signal processing algorithms, generation of radar measurements, and derivation of meteorological products) in a simulated environment. The polarimetric and Doppler observables are estimated based on the simulated radar voltages and presented in a plan position indicator (PPI) format. "True" fields of the corresponding radar observables are also produced on the same radar grid in order to check the performance of the signal processing procedures, as well as the effects related to the radar sampling volume. POWERS integrates the WRF input data with the T-matrix scattering method [20], in order to generate the polarimetric covariance matrix Σ of the cell(s) of interest. Propagation effects through the medium are also considered [6], [21]. The WRF model generates offline the microphysical parameters necessary to define the DSD, the distribution of the canting angle β, and the rotation angle α, along with wind speed and direction. The transmitted waveform is characterized by the pulsewidth T_0 (or, in general, by its bandwidth, if pulse compression signals are employed), and by the pulse repetition period T_s. The size of the RRV, which is proportional to the distance from the radar, is determined by the range resolution given by the radar pulse bandwidth and by the antenna aperture angles. Since it cannot be assumed, in general, that a weather phenomenon is homogeneous within an RRV, POWERS generates the radar signals as the superposition of radar echoes from a collection of a fixed number of sub-RRVs contained in the current RRV. The reference systems and the geometry are shown in Fig. 1. The sub-RRVs contributions are weighted with the appropriate value of the antenna radiation pattern, which is quite important when the antennas with large beamwidths are considered, as in the case of avionic radars. The subdivision is typically in azimuth and elevation only, since the subdivision along the range coordinate, though possible, increases the computational load.

The weather phenomenon is referred to the reference system (x, y, z) with an arbitrary origin (x_0, y_0, z_0), and the (x, y) plane parallel to the Earth′s surface. The radar reference system (x', y', z') is centered on the radar position (x_a, y_a, z_a) and is characterized by the elevation angle of the antenna θ_{el} with respect to the Earth′s surface. The nth sub-RRV is identified by a vector defined in the radar reference system. If each sub-RRV is sufficiently small compared to the extension of the weather phenomenon, the particles can be considered homogeneous within the sub-RRV. Under this hypothesis, the signal received from each RRV is the superposition of a large number of independent echoes backscattered by each particle in the RRV. Weather radars usually generate their integrated data using observation intervals (dwell times) not longer than fractions of 1 s, an interval during which the weather target can be assumed as stationary. In order to account for any possible polarimetric sequence in transmission, and assuming that linear horizontal (H) and vertical (V) polarizations are used, the simulation algorithm generates at every sweep the samples pertinent to all the three polarimetric channels (two for the copolar returns HH and VV and one for the crosspolar return, HV). More precisely, for the generic lth sub-RRV, three independent complex white Gaussian random sequences with zero mean and unit variance are generated. The sequences are then filtered by a Gaussian-shaped filter with appropriate central frequency (related to the mean Doppler speed of the particles $\mu_d^{(l)}$) and spectral width (related to the standard deviation of the Doppler speeds of the particles $\sigma_d^{(l)}$) to give the three channels the correct spectral shape. Indeed, the weather spectrum model chosen is Gaussian, which is correct in most cases even if in some occasions, it may be not accurate. This operation is repeated for every sub-RRV, weighted with the appropriate beam pattern value. The three time series are then mutually correlated via the Cholesky decomposition of the polarimetric covariance matrix Σ in order to produce signals with the correct amplitude and backscattering phase, as well as the proper mutual correlation properties. The resulting signals are then given as input to the radar signal simulation block, together with the range $r^{(l)}$ and the radar system constant $C = (\lambda G\sqrt{P_T})/(4\pi)$, where P_T, λ, and G are the pulse peak power, wavelength, and antenna gain, respectively. Finally, the received voltage time series $[V_{\mathrm{HH}}^{(l)}[m], V_{\mathrm{HV}}^{(l)}[m], V_{\mathrm{VV}}^{(l)}[m]]$, are generated, where $m = [0, \ldots, M-1]$ is the received sweep index. The simulator can also produce clutter echoes, which are of interest for the correct evaluation of signal degradation, especially at low elevations. Finally, POWERS can also simulate the pulse compression waveforms through waveforms such as chirp signals, Barker sequences, and PRB sequences.

B. Scenario Generation

The main ingredients needed to determine the polarimetric radar reflectivity are the normalized polarimetric radar cross section (RCS) of the hydrometeors of interest and their DSD. POWERS can generate simulated outputs at S-, C-, and X-frequency bands. As far as the use of the X-band is concerned, polarimetric Doppler weather radars operating in that band are employed because they are smaller, cheaper, and more sensitive to light rain, though the received signals are significantly affected by the attenuation induced by propagation in the precipitation medium, and their coverage is smaller. The reduced size and the still appropriate coverage make X-band the only candidate for avionic polarimetric Doppler radars. However, modeling the RCS of hydrometeors at X-band is harder than at C- or S- band, where the ratio between the average hydrometeor diameter

and the radar wavelength is small enough to fall within the Rayleigh scattering regime. This facilitates the computation of the normalized RCS because closed-form expressions are available even for nonspherical particles. At X-band, instead, the largest hydrometeors exhibit a higher diameter-to-wavelength ratio, so that the Mie scattering regime may apply. Therefore, numerical solutions are typically adopted to compute the RCS of hydrometeors at such frequencies.

We utilized the T-Matrix method, which is the fastest exact technique for the computation of nonspherical scattering based on a direct solution of Maxwell's equations. The T-Matrix can handle high-frequency scattering, however, problems of numerical convergence may show up when the diameter-to-wavelength ratio is too pronounced (especially for frequencies higher than 15 GHz). This issue, together with a complete description of the method, can be found in [20]. A remarkable feature is that the elements of the T-Matrix depend only on the wavelength and on the shape, size, and refractive index of the scattering particle. Consequently, the T-Matrix needs to be computed only once and can be successively used in computations for any wave incidence and scattering angle. Furthermore, the T-Matrix computed for an arbitrary orientation of a nonspherical particle can be directly used in the analytic computation of the scattering by randomly oriented particles. Note that though POWERS can simulate their scattering behavior, here, we do not consider multilayered ice particles or frozen particles, since the identification of a validation method that includes this type of hydrometeors is beyond the scope of this paper, which focuses on the case of rainfall.

The RCS pertinent to each of the three polarimetric channels is calculated from the corresponding element ($s_{\mathrm{HH}}, s_{\mathrm{VV}}$, and $s_{\mathrm{HV}} = s_{\mathrm{VH}}$) of the target scattering matrix $\mathbf{S}$ provided by the T-Matrix, as $\sigma_{\mathrm{HH/VV/HV}} = 4\pi |s_{\mathrm{HH/VV/HV}}|^2$. The three-component vector $\underline{S} = [s_{\mathrm{HH}}, s_{\mathrm{HV}}, s_{\mathrm{VV}}]$ is used to compute the polarimetric covariance matrix $\Sigma = \underline{S}^H \underline{S}$, where the superscript H denotes the conjugate transpose.

As far as the DSD is concerned, it is usually derived by disdrometer data fitting. Unfortunately, the results obtained are often valid only for the geographical area where data are collected and/or for a certain type of rainfall. The derived formulations are empirical, lacking generality. However, analytic DSDs based on real microphysical parameters exist [11], [18], and the WRF model is able to account for them. WRF is a state-of-the-art NWP code designed to serve both operational forecasting and atmospheric research needs. It features multiple dynamical cores, a 4-D variational data assimilation system, and a software architecture allowing for computational parallelism and system extensibility. It is developed and upgraded by a consortium of meteorological research organizations, among whom the National Center for Atmospheric Research, the National Oceanic and Atmospheric Administration (NOAA), and the University of Oklahoma. WRF is basically a regional NWP, meaning that it is conceived to achieve resolutions varying from 15 km to 1–2 km grid scale, but it is possible to work with higher resolution in a range from 300 to 1000 m in real-case simulations, depending on the resolution of the input sounding data.

Coherently, with numerous studies [22], we chose a Gamma DSD with arbitrary shape factor μ for every type of hydrometeor, namely

$$N(D) = N_0 D^{\mu} e^{-\Lambda D} \quad [\mathrm{m}^{-4}] \tag{1}$$

with slope

$$\Lambda = \left[\frac{\Gamma(4+\mu)\rho_r N_T}{6\Gamma(1+\mu)\rho_{\mathrm{air}} q_r} \right]^{\frac{1}{3}} \quad [\mathrm{m}^{-1}] \tag{2}$$

and intercept parameter

$$N_0 = \frac{N_T \Lambda^{1+\mu}}{\Gamma(1+\mu)} \quad [\mathrm{m}^{-4-\mu}] \tag{3}$$

where Γ is the Gamma function, ρ_r is the density of water in kg/m^3, N_T is the particle number concentration in m^{-3}, ρ_{air} is the air density in kg/m^3, and q_r is the rain mixing ratio (the ratio between the hydrometeors mass in a volume and the mass of dry air in that volume) in kg/kg. We used the Milbrandt–Yau microphysical model [23], which is a two-moment model capable of producing both the particle number concentration and the hydrometeor mixing ratio. Furthermore, it can handle hail separately and allows an easy tuning of the shape factors.

The reflectivity factors for the three channels Z_{HH}, Z_{VV}, and Z_{HV}, expressed in mm$^6 \cdot$ m^{-3}, are given by the following integral:

$$Z_{\mathrm{HH/VV/HV}} = 10^{18} \frac{\lambda^4}{\pi^5 |K_w|^2} \int_0^{\infty} \sigma_{\mathrm{HH/VV/HV}}(D) N(D) dD \tag{4}$$

where λ is the wavelength expressed in meters, $|K_w|^2 = 0.93$ is a function of the complex refractive index of water [3], D is the equivalent spherical diameter in meters, $\sigma_{\mathrm{HH}}(D)$, $\sigma_{\mathrm{VV}}(D)$, and $\sigma_{\mathrm{HV}}(D)$ are the RCSs expressed in m^2, and $N(D)$ is the DSD expressed in m^{-4}. We used the Beard and Chuang model to describe the hydrometeors shape [24].

Since the reflectivity factors (in particular the copolar ones) may vary by several orders of magnitude, they are expressed in logarithmic scale as dBZ. In particular, Z_{HH} expressed in dBZ is referred to as absolute reflectivity. The other polarimetric observables that POWERS is able to generate are as follows.

1) Differential reflectivity (in decibels)

$$Z_{\mathrm{DR}} = 10 \cdot \log_{10} \left[\frac{Z_{\mathrm{HH}}}{Z_{\mathrm{VV}}} \right]. \tag{5}$$

2) Linear Depolarization Ratio (in decibels)

$$\mathrm{LDR} = 10 \cdot \log_{10} \left[\frac{Z_{\mathrm{HV}}}{Z_{\mathrm{HH}}} \right]. \tag{6}$$

3) Specific Differential Phase (in deg/km)

$$K_{\mathrm{DP}} = 10^3 \frac{2\pi}{k_0} \cdot \Re \left\{ \int_0^{\infty} [f_{\mathrm{HH}}(D) - f_{\mathrm{VV}}(D)] dD \right\} \tag{7}$$

where k_0 is the propagation wavenumber in vacuum, $\Re$ denotes the real part, while $f_{\mathrm{HH}}(D)$ and $f_{\mathrm{VV}}(D)$ are the forward scattering matrix elements (i.e., the elements of $\mathbf{S}$ still estimated via the T-Matrix method, but with a bistatic angle of 180° rather than 0°, with reference to the conventional backscattering agreement) [22].

4) Copolar Correlation Coefficient

$$\rho_{\mathrm{HV}} = \frac{s_{\mathrm{HH}} \cdot s_{\mathrm{VV}}^{*}}{\sqrt{|s_{\mathrm{HH}}|^2 |s_{\mathrm{VV}}|^2}}. \tag{8}$$

III. First Validation Check: Sun and Crook Relation

As mentioned earlier, POWERS is able to account for different kinds of hydrometeors and heterogeneous phenomena, while the microphysical parameters necessary to build the DSD are provided by the WRF model. In order to reproduce the simplest possible physical environment that should serve as reference "truth", the rain mixing ratio q_r and the number concentration N_T were forced to be constant within the entire scenario. This implies a constant value of the water mass in the simulation, and, consequently, a constant value of the absolute reflectivity was expected. However, to be able to assess that the constant Z_{HH} generated by POWERS in all RRVs is physically consistent (namely, consistent with the WRF input to the radar simulator), a relation between Z_{HH} and q_r is needed. Indeed, in the literature, there is no theoretically derived relations of that kind, but there are empirical formulas that are widely accepted by the meteorological community, since they are typically used for assimilation of Doppler radar data in atmospheric prediction models [1], [2], [25].

That described in [25] is a common procedure used for weather radar data assimilation, and, therefore, can be exploited to retrieve the absolute reflectivity from the total precipitation concentration (i.e., the water content) directly from the mixing ratio or from the DSD parameters. The interdependency between Z_{HH} and q_r is also supported by the fact that in some cases (see for instance [5]), it is exploited by the radar signal simulators to generate the amplitude of the scattered field for a given scenario. More interestingly, for our purposes, some power-law relationships exist that are valid for all types of hydrometeors in both the Rayleigh and the Mie scattering regimes, and that relate the physical features of the phenomena to their intensity (for instance [25]–[27]). Among them, we chose that proposed by Sun and Crook [28]. They demonstrated that the state variables in a cloud-scale model with rain parameterization could be initialized using a 4-D-Var Doppler Radar Analysis System, which assimilated the Doppler radar observations. In this manner, they derived the following relationship between the absolute reflectivity[1] and the mixing ratio, for rainfall and Rayleigh scattering, assuming a Marshall–Palmer (MP) DSD [29]

$$Z_{\mathrm{HH}}[\mathrm{dBZ}] = 43.1 + 17.5 \log_{10}(\rho_{\mathrm{air}} q_r) \tag{9}$$

where q_r is in g/kg and ρ_{air} is in kg/m^3.

The work by Sun and Crook [28] provides an interesting way to assess the consistency of POWERS outputs. In fact, based on (9), to a given quantity of hydrometeors (expressed through the mixing ratio) must correspond a given constant value of reflectivity. Therefore, (9) could be used as a physically consistent reference to check the quality of the simulation outputs and also to determine the value of q_r to initialize POWERS, as discussed in the following.

[1]Note: single (horizontal)-polarization radar data were assimilated

TABLE I
Reference Absolute Reflectivities and Related POWERS Inputs

Case	Simulator inputs	
Z_{HH}[dBZ]	q_r [kg/kg]	N_T [mm^{-3}]
30	$1.78 \quad 10^{-4}$	$2.32 \quad 10^{3}$
35	$3.44 \quad 10^{-4}$	$2.73 \quad 10^{3}$
40	$6.65 \quad 10^{-4}$	$3.23 \quad 10^{3}$
45	$1.30 \quad 10^{-3}$	$3.80 \quad 10^{3}$
50	$2.50 \quad 10^{-3}$	$4.48 \quad 10^{3}$
55	$4.80 \quad 10^{-3}$	$5.28 \quad 10^{3}$
60	$9.21 \quad 10^{-3}$	$6.23 \quad 10^{3}$

A. Constant Rainfall Scenario and Simulation Setup

Before running POWERS, we selected seven reflectivities from which we derived the corresponding values of the mixing ratio q_r through (9). We then used these values as input to POWERS for 14 different simulation runs (7 at S-band and 7 at X-band). The absolute reflectivity values considered range from 30 to 60 dBZ by steps of 5 dBZ, and the frequencies selected are 3.0 GHz (S-band) and 9.4 GHz (X-band).

We set $\rho_{\mathrm{air}} = 1$ kg/m^3 and $\rho = 10^3$ kg/m^3 for simplicity; otherwise, we would get different meteorological features within each RRV due to the height of the RRV and to its volume (both increasing with the distance from the radar). In order to reproduce the MP hypothesis, we set $N_0 = 8000$ m^{-4} and $\mu = 0$, considering only liquid precipitation. N_T and Λ were computed through (2) and (3). Table I illustrates the seven q_r-N_T pairs obtained in this manner (the values of Λ are not shown, since Λ is not a simulator input). These values became the meteorological inputs of the aforementioned POWERS simulations.

B. Results

For validation purposes, the following three different reflectivities have been considered and plotted in Fig. 2 versus the mixing ratio.

1) The theoretical reflectivity derived from the Sun and Crook [28] formula of (9) (black dashed curves).
2) The "true" reflectivity provided by (4), with N_T and q_r constituting the reference "truth" parameters since they are given as input to POWERS (continuous red curves).
3) The "simulated" reflectivities obtained by processing an I and Q time series corresponding to 2800 integrated samples (blue stars).

Note first that the reflectivities 1) and 2) behave differently at the two frequencies. In fact, Fig. 2(a) shows that the Sun and Crook relation tends to slightly underestimate the "true" reflectivities in the S-band, with an error increasing with the rain mixing ratio. In the X-band, instead, Fig. 2(b) indicates that the Sun and Crook relation tends to a slight overestimation, with a greater error for smaller rain mixing ratios. However, in both cases, the differences are smaller than 1 dBZ, meaning that q_r and N_T (i.e., the meteorological parameters used as input to the simulator) generate absolute reflectivities that are consistent with those predicted by (9). The observed errors could be attributed to the hypotheses about the hydrometeors' shape used to compute Z_{HH}. In fact, as previously mentioned, the Beard and Chuang model was

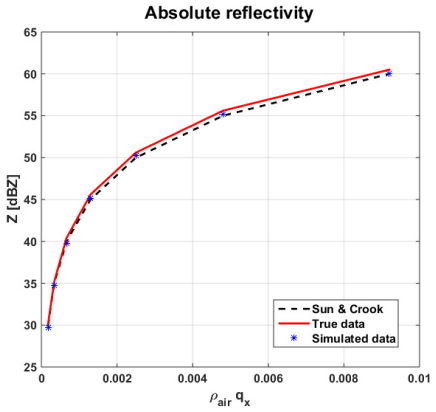

(a)

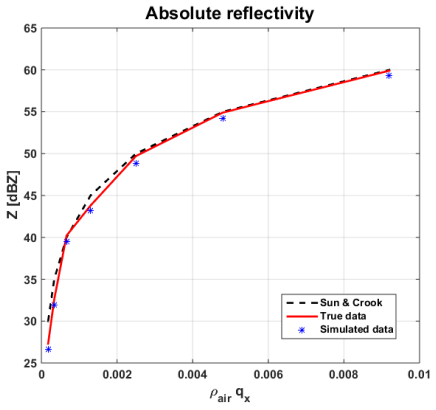

(b)

Fig. 2. Absolute reflectivity versus rain mixing ratio for 3 GHz (S-band) and 9.4 GHz (X-band). Dashed curves: curves obtained using the Sun and Crook relation (9). Continuous curves: reflectivity values provided by (9) using the "true" reference parameters provided as input to POWERS. Blue stars: simulated reflectivities obtained by processing the I and Q signals generated by POWERS. (a) S-band. (b) X-band.

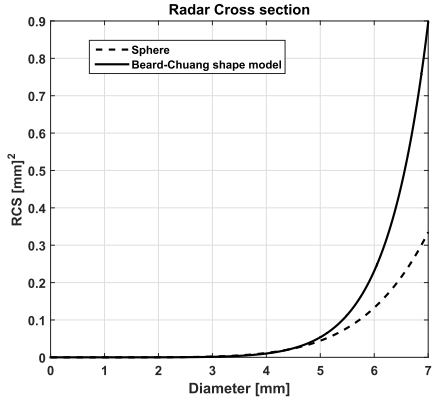

Fig. 3. Comparison between the RCS of a water sphere (dashed curve) and that of an oblate hydrometeor (continuous curve) in the Rayleigh scattering regime.

adopted for (4), while (9) was derived assuming a spherical model. The impact of the shape model on the RCS, and, consequently, on the absolute reflectivity is well illustrated by Fig. 3, which plots the RCS of a spherical droplet (dashed curve) and that of an oblate droplet (continuous curve) versus the equivalent diameter.

TABLE II

SIMULATED POLARIMETRIC OBSERVABLES AT S-BAND

	S band - Rain Cases						
Sun & Crook	**30 dBZ**	**35 dBZ**	**40 dBZ**	**45 dBZ**	**50 dBZ**	**55 dBZ**	**60 dBZ**
Z_{HH}[dBZ]	29.7	34.7	39.8	45.1	50.2	55.2	60.0
Z_{DR}[dB]	0.7	1.0	1.3	1.8	2.3	2.9	3.5
LDR [dB]	-37.7	-34.0	-31.5	-29.2	-27.4	-25.9	-24.7
K_{DP}[deg/km]	0.03	0.05	0.20	0.4	1	2.7	7.20
ρ_{HV}	0.99	0.99	0.99	0.99	0.98	0.98	0.97

TABLE III

SIMULATED POLARIMETRIC OBSERVABLES AT X-BAND

	X band - Rain cases						
Sun & Crook	**30 dBZ**	**35 dBZ**	**40 dBZ**	**45 dBZ**	**50 dBZ**	**55 dBZ**	**60 dBZ**
Z_{HH}[dBZ]	26.6	31.9	39.5	43.2	48.8	54.2	59.3
Z_{DR} [dB]	0.82	1.2	2.2	2.4	2.9	3.6	4.1
LDR [dB]	-34.7	-31.5	-27.5	-27.0	-25.4	-24.4	-23.6
K_{DP} [deg/km]	0.04	0.11	0.41	0.87	2.25	5.6	7.3
ρ_{HV}	0.99	0.99	0.99	0.99	0.98	0.98	0.98

More importantly, note that the simulated reflectivities (blue stars) are close to the "true" ones both in Fig. 2(a) and (b), which means that POWERS can simulate signals that are consistent with both the "truth" reference and the physical meteorological inputs.

The Sun and Crook relation involves only the absolute reflectivity. Therefore, there is no possibility to adopt an analogous procedure to assess the quality of the other polarimetric outputs. However, observing Tables II and III that show the mean values of all the polarimetric variables calculated on 100 RRVs at both frequency bands, it can be noted that the behavior of the simulated polarimetric variables is coherent with that typically observed in rainfall. In fact: 1) the differential reflectivity Z_{DR} and the differential propagation phase constant K_{DP} increase with increasing Z_{HH}; 2) LDR decreases with decreasing Z_{HH} (namely, as the raindrops become smaller and their shape gets closer to spherical); and 3) ρ_{HV} decreases slightly with increasing Z_{HH}, since the two backscattered signals at orthogonal polarizations lose some correlation as the rainfall gets more intense [30].

IV. SECOND VALIDATION CHECK: REAL DSD PARAMETERS AS POWERS INPUTS

The validation method presented in this section is still based on a constant scenario evaluating POWERS outputs. However, the meteorological inputs are not chosen according to a reference formula that connects a radar observable to the precipitation microphysics, but are directly estimated from real DSD data acquired by disdrometers.

A. Data Set

The real DSD data we utilized come from the [Hydrological cycle in the Mediterranean Experiment (HyMeX), www.hymex.org] experimental program carried out in Autumn 2012 with the purpose to better understand the water cycle in the Mediterranean, with particular emphasis on extreme events [31]. HyMEX selected three main Mediterranean target areas: Northwest, Adriatic, and Southeast. In particular, three Italian hydrometeorological monitoring sites were identified: Liguria-Tuscany, Northeastern Italy, and Central Italy.

Within each target area, several hydrometeorological sites for monitoring heavy rainfall and flash flooding were set up. The observation strategy of HyMEX has been organized in a long-term (4 years) enhanced observation period and short-term (2 months) special observation period (SOP).

The data we selected belong to the Rome SOP, which lasted from September to November 2012. The samples were gathered by means of a laser-optical Parsivel disdrometer, installed on the roof of the Department of Electrical Engineering and Telecommunications of La Sapienza University in Rome, Italy (41.89N, 12.49E, 70 m above sea level). A detailed description of the instrumentation used for HyMeX SOP 1 in Central Italy can be found in [32].

In particular, we focused on 50 measurements made between 18:00 and 19:00 UTC of October 15, 2012. During that hour, a cyclone grew over the Gulf of Genoa and the associated frontal system moved rapidly toward the Italian peninsula, causing moist air advection over the Tyrrhenian Sea and consequent deep convection on the Tyrrhenian coast. In particular, a convective storm affected the city and region of Rome (the same that will be examined with reference to the third validation check).

B. Procedure and Results

The Parsivel disdrometers characterize the DSD in a 32×32 matrix (32 fall speed classes versus 32 size classes). The temporal resolution is configured as 10 s and the total number of disdrometer samples available in the aforementioned hour is 360. We selected a representative subset of 50 among these, as this was deemed a sufficient number for our test aimed at analyzing the behavior of the simulator.

The 50 disdrometer samples selected were processed by means of the T-matrix method [33] both at 3.0 and 9.4 GHz, with the purpose to estimate the absolute and differential reflectivities Z_{HH} and Z_{DR}. The results are shown in Fig. 4. The drop shape model we used is that by Brandes *et al.* [34], while the temperature was measured by a local sounding station.

In the observation interval, rain rates up to 16 mm/h were measured, as evidenced by the scatterplots of Fig. 4. Note the typical signature of rainfall: Z_{HH} ranging between 0 and 55 dBZ and Z_{DR} that correspondingly increases up to 4.5 dB, with a spread that increases with increasing rainfall rates.

The same 50 samples were then processed to extract all the DSD parameters necessary to feed POWERS. Specifically, for each sample, we computed the couple $(q_r,\ N_T)$ in order to define a weather scenario consistent with that from which the real data were acquired. The equivalent volume diameter D_0, (defined so that drops with a diameter less than D_0 contribute to half the total rainwater content W [22]) was found through the relations

$$\frac{\pi}{6}\rho_w \int_0^{D_0} D^3 N(D) dD = \frac{1}{2} W \tag{10}$$

$$W = \frac{\pi}{6}\rho_w \int_0^{\infty} D^3 N(D) dD \quad [\mathrm{g \cdot m^{-3}}] \tag{11}$$

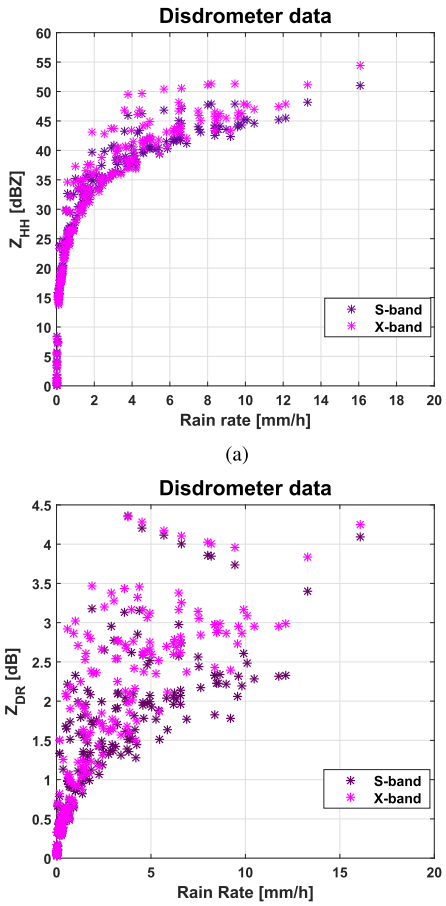

Fig. 4. (a) Scatterplot shows the values of absolute reflectivity versus rain rate at both 3.0 GHz (S-band) and 9.4 GHz (X-band), estimated from the real DSD data acquired during the HyMeX activity of October 15, 2012 in Rome, Italy. (b) Scatterplot shows the values obtained for the differential reflectivity at the same frequencies.

where D is the raindrop equivalent diameter (expressed in millimeters), ρ_w is the water density ($1\ \mathrm{g \cdot cm^{-3}}$). The DSDs were fitted by a normalized Gamma model in order to easily account for different water contents [22], [35]

$$N(D) = N_w f(\mu) \left(\frac{D}{D_0}\right)^{\mu} \exp\left[-(3.67+\mu)\frac{D}{D_0}\right] \tag{12}$$

with

$$f(\mu) = \frac{6}{(3.67)^4} \frac{(3.67+\mu)^{\mu+4}}{\Gamma(\mu+4)}. \tag{13}$$

The normalized intercept parameter N_w $[\mathrm{mm^{-1} m^{-3}}]$ was estimated based on W and D_0

$$N_w = \frac{3.67^4}{\pi \rho_w} \left(\frac{10^3 W}{D_0^4}\right). \tag{14}$$

Recalling that N_w is related to N_0 of (3) as follows:

$$N_0 = N_w f(\mu) D_0^{-\mu} \quad [\mathrm{mm^{-1-\mu} m^{-3}}]. \tag{15}$$

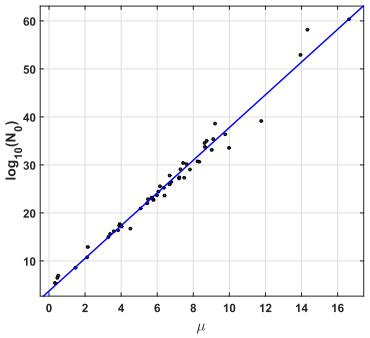

Fig. 5. Black dots: values of N_0 determined from the real DSD data versus μ calculated through (18). Blue line: regression line.

The number concentration and the mixing ratio were calculated through (2) and (3)

$$N_T = \frac{N_0 \Gamma(1+\mu)}{\Lambda^{1+\mu}} \tag{16}$$

$$q_r = \frac{\Gamma(4+\mu)\rho\pi N_0}{6\rho_{\text{air}}\Lambda^{1+\mu}}. \tag{17}$$

Finally, the shape parameter μ was estimated following the work by Ulbrich and Atlas [36]. They identified a relation between μ and a combination of DSD moments, which is valid for $\mu \geq -3.63$, viz

$$\mu = \frac{(7-11\eta) - [(7-11\eta)^2 - 4(\eta-1)(30\eta-12)]^{1/2}}{2(\eta-1)} \tag{18}$$

where η was calculated as

$$\eta = \frac{p_4^2}{p_2 p_6} = \frac{[\Gamma(5+\mu)]^2}{\Gamma(3+\mu)\Gamma(7+\mu)} = \frac{(3+\mu)(4+\mu)}{(5+\mu)(6+\mu)} \tag{19}$$

where $p_n = \int D^n N(D) dD$ being the nth moment of the DSD.

Fig. 5 shows the scatterplot between $\log_{10}(N_0)$ and μ obtained through the described procedure. Note that N_0 reaches very large values, which is a typical feature of this parameter since there is a strong correlation between $\log_{10}(N_0)$ and μ [36]. This is evidenced by the regression line of Fig. 5 and by the correlation coefficient that is higher than 0.98. However, as shown in [22], such correlation is not due to a real physical interdependence between the two parameters, but to the fact that N_0 involves the quantities that depend in turn ON μ.

The other microphysical parameters needed to initialize POWERS, such as the water density and the density of the air, have been set constant for the sake of simplicity. The radar system parameters used for all simulations are reported in Table IV.

One simulation was carried out for each of the 50 couples (N_T, q_r), setting each time the proper value of μ, and for each of the two frequencies considered. The absolute and differential reflectivities simulated by POWERS (blue stars) are shown in Fig. 6, together with those computed directly from the real DSD data (red diamonds). At both S- and X-bands, the simulated output data are in very good agreement with those derived from the real data. Despite some outliers, the two plots feature the typical $Z_{\text{HH}} - Z_{\text{DR}}$ signature in rainfall.

TABLE IV
RADAR PARAMETERS FOR SIMULATIONS

Antenna	**S band**	**X band**
Shape	Gregorian Parabolic	
Diameter	8.5 m	
Gain	43 dBi	53 dBi
Beamwidth (3dB)	1 deg	0.3 deg
Antenna rotation vel.	1.74 rounds/min	0.83 rounds/min
Max SLL	< -33 dB	< -36 dB
Transmitters		
Frequency	2.725 GHz	9.41 GHz
Peak Power	1 MW	250 kW
PRF max	1250 Hz	2000 Hz
Duty cycle	0.16%	
Range Resolution	192 m	120 m
Receivers		
Noise figure	3.4 dB	4.0 dB
Noise power	-114 dBm	
Dynamic range	80 dB	90 dB

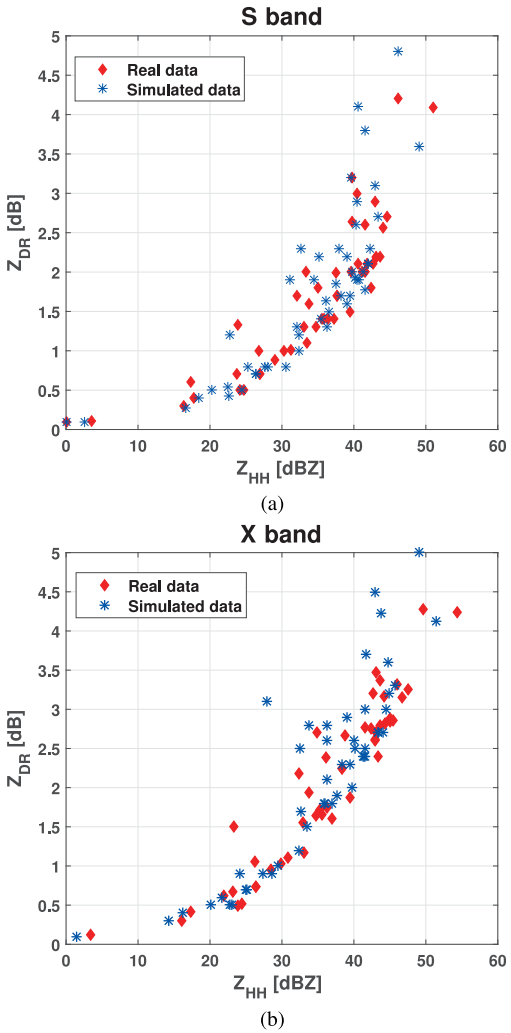

Fig. 6. Scatterplots of Z_{HH} versus Z_{DR} computed at (a) 3 GHz and (b) 9.4 GHz based on the 50 DSD samples recorded at 18:00-19:00 UTC of October 12, 2012 in Rome (red diamonds), and simulated by POWERS using the microphysical inputs derived from the same 50 DSD samples (blue stars).

It is also worth noticing that the correlation between the simulated data at the two frequencies is very high. Though each DSD parameter was forced to vary in a wide range of values ($0.63 \leq D_0 \leq 4.86$ mm, $1 \leq \log_{10} N_w \leq 3$, and $0.3 \leq \mu \leq 16$ for $R < 20$ mm h^{-1}), Z_{HH} and Z_{DR} at the two frequencies are tightly related, as shown by Fig. 7(a) and (b).

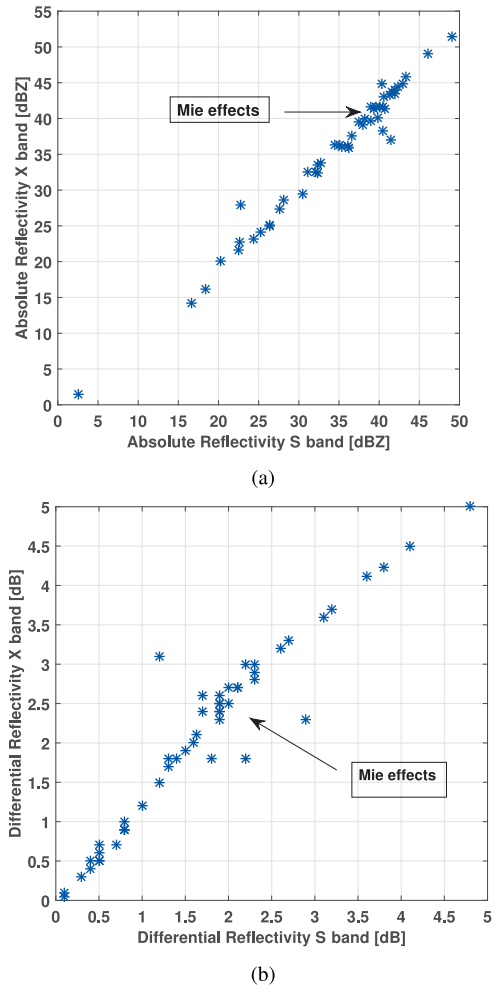

Fig. 7. Comparison between the (a) absolute and (b) differential reflectivities simulated at S- and X-bands. Some effects of Mie scattering computations are evidenced.

The small clusters around 40 dBZ in Fig. 7(a) and around 2.0–2.5 dB in Fig. 7(b) are due to Mie scattering. Indeed, under the Rayleigh scattering hypothesis, Z_{HH} and Z_{VV} are independent of frequency. However, such hypothesis may not be always correct at X-band [37] and Mie scattering should be accounted for. In this case, since closed-forms for the RCS of the hydrometeors are not available for the Mie scattering region, the T-matrix method adopts numerical solutions that may result in slight oscillations around the expected values, as the simulation settings are varied.

V. Third Validation Check: WRF Scenario as POWERS Input

The validation approach presented in the following aims at checking the consistency of POWERS outputs in a more complex environment. The 3-D scenario, in this case, is under the control of the NWP model, without any kind of limitation.

A. Procedure

An NWP-based simulator is conceived to generate radar measurements that are consistent with the quantity of precipitating hydrometeors of the synthetic meteorological scenario. In our case, the mass of precipitating liquid water provided by WRF serving as "truth" reference was compared to the estimates derived from the simulated weather radar acquisition process. More precisely, since the main observable is the absolute reflectivity, which is related to the backscattered power per unit volume we considered the rainwater content per unit volume W. Since the WRF model provides the mixing ratio (see 17), W is calculated as $W = q_r \cdot \rho_{\mathrm{air}}$.

B. Simulation Settings

We applied this method to two different weather scenarios, the first simulated at X-band and the second at S-band and we considered only the liquid part of the precipitation. The first case study is a heavy rainfall that hit Florence (Italy) on August 1, 2015. The second one is an intense convective event that took place in the afternoon of October 15, 2012 in the Rome area, namely, the same event mentioned in Section IV. The WRF model code regenerated the two events from 00:00 UTC to 24:00 UTC, with a 20-min time step over a 375 m $\times$ 375 m grid. Both were processed by the WRF model by using real atmospheric parameters measurements that are made available as GRIdded Binary files, provided by the National Centers for Environmental Prediction data archives [16]. In both cases, the DSD shape parameter μ was set equal to 2.2. The radar parameters are the same used in the second check (see Table IV) and each RRV was subdivided along azimuth and elevation, but not along the range. The sub-RRVs have an angular width of 1/6 of the antenna aperture, i.e., 0.167° at S-band and 0.05° at X-band.

C. Florence Case Results

The Florence scenario is characterized by a high melting layer (up to 3750 m) and by a fair concentration of precipitable water with a mixing ratio up to 1 g/kg. Above the melting layer, there is also a noticeable amount of iced precipitation. The extent of the phenomenon is about 4000 km^2.

The radar simulations were carried out by POWERS assuming to use an X-band polarimetric radar with the characteristics reported in the first column of Table IV, located in Florence (43° 46' 10.42' North Latitude, 11° 15' 20.9304' East Longitude) and the radar coverage is about 100 km. Attenuation due to propagation in the rainfall medium was intentionally neglected since it would have biased our analysis, as will come out clearly in the following. Fig. 8(a) shows the "true" absolute reflectivity, directly estimated from the truth reference provided by WRF, while Fig. 8(b) shows the spatial distribution of W computed in each volume as explained previously.

The reflectivity factor Z_{HH} is highly correlated with W and their mutual dependence can be expressed as

$$Z_{\mathrm{HH}} = a W^b. \tag{20}$$

Fig. 9 shows, for the scenario under test, the "true" absolute reflectivity Z_{HH} (dBZ) versus $\log_{10}(W)$ calculated directly from the WRF output. We computed the linear regression between them, getting $a = 3.03 \cdot 10^9$ and $b = 1.606$, having expressed W in kg/m^3. Equation (20) was then used to estimate the water density $\widehat{W}$ from the absolute reflectivity $\widehat{Z_{\mathrm{HH}}}$ simulated by POWERS. In this manner, we obtained

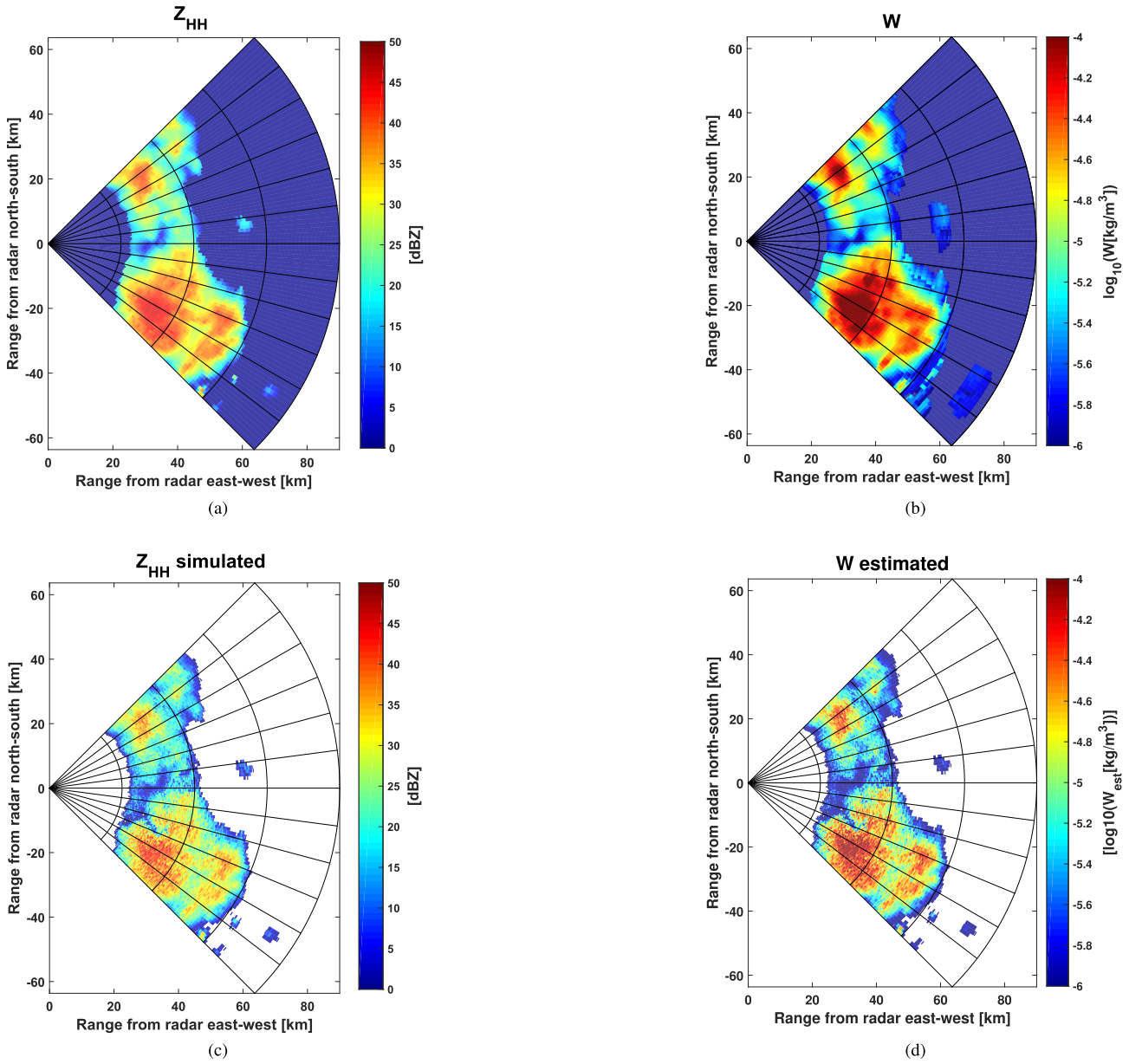

Fig. 8. PPI plots for the Florence scenario. (a) "True" absolute reflectivity, calculated by means of the "truth" reference provided by WRF. (b) $\log_{10}(W)$ [kg/m^3]) directly estimated from the WRF output. (c) Absolute reflectivity simulated by POWERS ($\widehat{Z_{\rm HH}}$). (d) Rainfall water content estimated by inverting (20) and using the simulated reflectivity $\widehat{Z_{\rm HH}}$ as input.

the two PPI plots of Fig. 8(c) and (d), showing $\widehat{Z_{\rm HH}}$ and $\widehat{W}$, respectively. The histogram of the percentage error made when estimating the water content through $\widehat{Z_{\rm HH}}$ and (20) is shown in Fig. 10. Note that the majority of the samples exhibit an error smaller than 7%, which denotes a very good consistency between the simulated and "true" values of W.

A further demonstration that the simulated radar observables are fully coherent with the meteorological context where they have been generated is given by Fig. 11, which plots $Z_{\rm DR}$ versus the mass-weighted mean diameter D_m of the DSD, defined as

$$D_m = \frac{\int_0^\infty D^4 N(D) dD}{\int_0^\infty D^3 N(D) dD}. \tag{21}$$

We recall that $\Lambda(D_m - D_0) = 0.33$ for a Gamma DSD [22]. It can be easily verified that scatterplot in Fig. 11 is in excellent agreement with that reported in [22, Fig. 7.20]. Finally, in view of the following comparison with the Rome case results, it is opportune to note that the values of D_0 for this scenario are smaller than 2.5 mm.

D. Rome Case Results

The second case investigated is the storm that occurred over the Rome regional area on October 15, 2012 (a PPI scan of $Z_{\rm HH}$ is shown in Fig. 12). Compared to the Florence case, it has a wider extent (about 48 000 km^2). In this case, POWERS simulated an S-band polarimetric radar operating

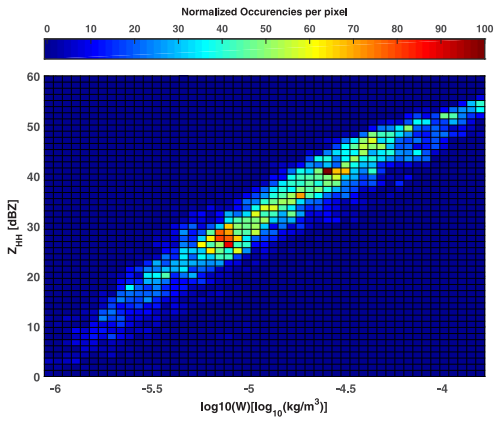

Fig. 9. Regression between the true absolute reflectivity and W estimated from WRF, in logarithmic scale.

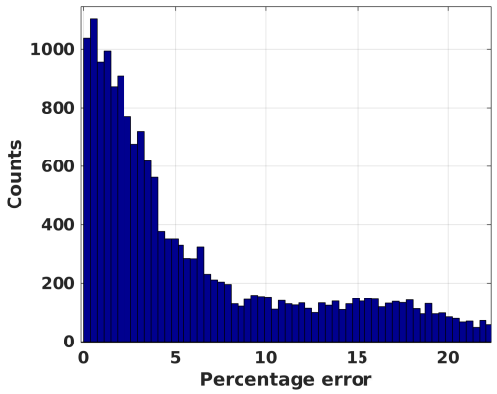

Fig. 10. Distribution of the percentage error between the estimated and "true" values of W [kg/m^3] (Florence case).

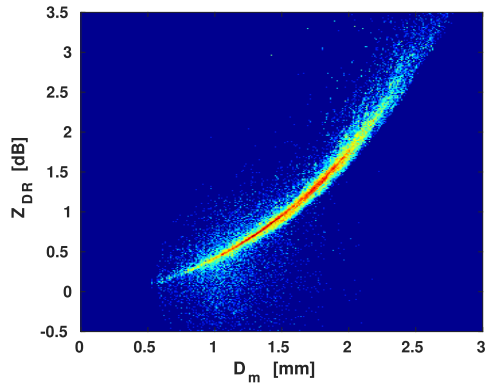

Fig. 11. Z_{DR} versus D_m (Florence case).

with the parameters listed in the second column of Table IV and sited in Rome (41° 50' 24" North latitude, 12° 38'50" East Longitude) at 102 m above sea level.

The large spread of the values of the hydrometeors equivalent diameters, well evidenced by Fig. 13, indicates that this event is highly convective. A more accurate analysis of the simulated microphysical parameters revealed that the storm consists of two different types of precipitation: one medium intensity (D_0 up to about 2.5 mm) and a strong convective one (2.5 mm $< D_0 <$ 7 mm). For this reason, we have split the two storm components and carried out the analysis only

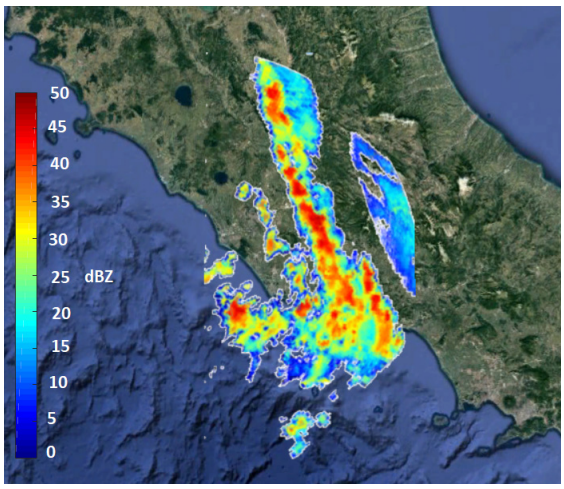

Fig. 12. Absolute reflectivity map of the rainstorm that hit the city and region of Rome on October 15, 2012.

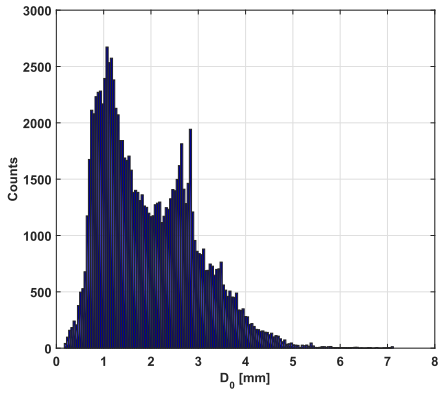

Fig. 13. Histogram of the equivalent volume drop diameters derived from the WRF scenario (Rome case).

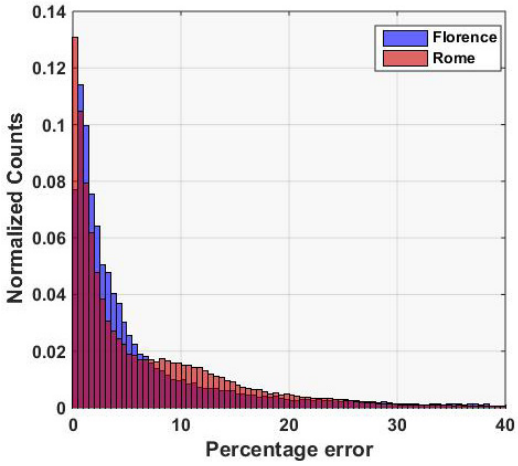

Fig. 14. Normalized distribution of the percentage error between the estimated and "true" values of $W[kg/m^3]$ for the Florence (blue) and Rome (red) cases.

on the first one. In fact, besides examining separately storm elements with different microphysical nature, the purpose was to make a comparative analysis with respect to the Florence case that, as mentioned, presented a similar range of values of D_0, albeit with a different distribution.

The procedure of estimating $\widehat{W}$ from the simulated $\widehat{Z_{\mathrm{HH}}}$ was the same applied in the Florence case. For the sake of comparison, we report in Fig. 14 the normalized version of the percentage error occurrences of the Florence case together with those of the Rome case. The separate analysis of the first component of the storm has allowed us to highlight that the distribution of the percentage error and its values closely resemble those of the Florence case, evidencing that the POWERS outputs are robust and well consistent with the physical inputs provided by WRF.

VI. Conclusion

We have presented a procedure that has been applied to the outputs of the newly developed NWP-based polarimetric Doppler weather radar signals simulator called POWERS. The goal of the procedure is checking the ability of the simulator to generate radar signals that are consistent with the input in the case of rainfall. The procedure is articulated around three check levels, whose common ground is the need to assess the consistency of the POWERS outputs with respect to the microphysical parameters referrable to the specific NWP model used as input (WRF in our case). This is not a straightforward task since it asks for relating an input weather scenario to an output which has a totally different nature, being generated after proper simulation and processing of radar signals. For this reason, the procedure consists of a first basic check level characterized by a fully controlled, spatially constant synthetic scenario in place of a realistic one generated by WRF, then it goes through a second check level where the scenario is still constant but the microphysical data are deduced from real measurements, while the realistic and heterogeneous weather environment represented by the WRF inputs to POWERS is considered only in the third and last check. All these checks demonstrated that POWERS is robust and able to simulate radar observables that are consistent with the NWP inputs through which POWERS generates its polarimetric signals.

Note that though POWERS can simulate signals for every class of hydrometeors, we have limited our analysis to rainfall because in this case, we could ground the validation checks on a well-established basis. This is true in particular for the first two checks. In fact, regarding the first one, the Sun and Crook relation is valid only in rainfall (besides involving only the absolute reflectivity). With regard to the second one, the DSD measured by Parsivel disdrometers is accurately defined in rainfall, while the limitations and pitfalls have been clearly evidenced in the case of solid precipitation [40], not to mention the fact that the density of solid hydrometeors is unknown.

It is worth mentioning that some attempts were made not only to validate the POWERS outputs in nonrainfall cases [19], [21], [38] but also to validate a precipitation classification algorithm through POWERS simulations [39]. Nevertheless, much more efforts are needed to approach the final objective we are pursuing, which is to validate POWERS in the general case of nonrainfall precipitation. The task is complex indeed, but at the same time, it is of the maximum concern in particular for the avionic sector. Recent documents of the European Organization for Civil Aviation Equipment available https://www.rtca.org/content/sc-230 indicate that single-polarization radars are not effective to detect ice since "there is no reasonable relationship between reflectivity and ice water content", and reveal a strong interest to investigate accurately the benefits that polarimetry could bring for the detection of hail and icing phenomena. In particular, the latter can be even more dangerous than hail since they occur when the air contains droplets of supercooled liquid water that cannot be detected by X-band radars but cause the formation of ice on the aircraft sensors and surface. Though such droplets cannot be detected, a polarimetric radar has the potential to infer their presence, as we showed in [41] using ground-based weather radars. This poses new interesting research challenges in the sector. However, the organization of measurement campaigns aimed at validating hydrometeors classification methods to be applied on board civil aircraft is extremely complicated due to the impossibility to set up any truth reference aloft. In such a context, the development and validation of simulation tools such as POWERS for hydrometeors classification is an option of the utmost importance for the progress of the research aimed at pilots' risk awareness and flight safety.

References

[1] J. Gao and D. J. Stensrud, "Assimilation of reflectivity data in a convective-scale, cycled 3DVAR framework with hydrometeor classification," *J. Atmos. Sci.*, vol. 69, pp. 1054–1065, Mar. 2012.

[2] D. C. Dowell, L. J. Wicker, and C. Snyder, "Ensemble Kalman filter assimilation of radar observations of the 8 May 2003 Oklahoma City supercell: Influences of reflectivity observations on storm-scale analyses," *Monthly Weather Rev.*, vol. 139, no. 1, pp. 272–294, July 2011.

[3] J. D. Doviak and D. S. Zrnić, *Doppler Radar and Weather Observations*, 2nd ed. New York, NY, USA: Academic, 1993.

[4] M. D'Amico *et al.*, "The X-WALD project: Towards a cleaner sky," in *Proc. 44th Eur. Microw. Conf.*, Oct. 2014, pp. 585–588.

[5] B. L. Cheong, R. D. Palmer, and M. Xue, "A time series weather radar simulator based on high-resolution atmospheric models," *J. Atmos. Ocean. Technol.*, vol. 25, no. 2, pp. 230–243, Feb. 2008.

[6] S. Lischi, A. Lupidi, M. Martorella, F. Cuccoli, L. Facheris, and L. Baldini, "Advanced polarimetric Doppler weather radar simulator," in *Proc. 15th Int. Radar Symp. (IRS)*, Jun. 2014, pp. 1–6.

[7] S. Lischi, "Advanced Doppler polarimetric weather radar simulation and processing," Ph.D. dissertation, Dept. Inf. Eng., Univ. of Pisa, Italy, May 2016.

[8] A. Lupidi, S. Lischi, F. Berizzi, M. Martorella, and F. Cuccoli, "Polarimetric avionic weather radar for increasing flight safety and efficiency," in *Proc. 29th Congr. Int. Council Aeronaut. Sci. (ICAS)*, 2014, pp. 1–8.

[9] A. D. Byrd *et al.*, "A weather radar simulator for the evaluation of polarimetric phased array performance," *IEEE Trans. Geosci. Remote Sens.*, vol. 54, no. 7, pp. 4178–4189, Jul. 2016.

[10] C. Capsoni, M. D'Amico, and R. Nebuloni, "A multiparameter polarimetric radar simulator," *J. Atmos. Ocean. Technol.*, vol. 18, no. 11, pp. 1799–1809, Nov. 2001.

[11] Z. Li, Y. Zhang, G. Zhang, and K. A. Brewster, "A microphysics-based simulator for advanced airborne weather radar development," *IEEE Trans. Geosci. Remote Sens.*, vol. 49, no. 4, pp. 1356–1373, Apr. 2011.

[12] R. M. May, "Estimating and mitigating errors in dual-polarization radar attenuation correction," Ph.D. dissertation, School Meteorol., Univ. Oklahoma, Norman, OK, USA, 2014.

[13] D. S. Zrnić, "Simulation of weatherlike Doppler spectra and signals," *J. Appl. Meteorol.*, vol. 14, no. 4, pp. 619–620, Jan. 1975.

[14] A. Lupidi, S. Lischi, F. Cuccoli, F. Berizzi, and L. Facheris, "Capabilities and potential of an avionic polarimetric weather radar simulator," in *Proc. Signal Process. Symp. (SPSympo)*, Jun. 2015, pp. 1–5.

[15] W. C. Skamarock *et al.*, "A description of the advanced research WRF version 3," NCAR Tech. Note NCAR/TN-475+STR, 2008, p. 113, doi: 10.5065/D68S4MVH.

[16] *National Centers for Environmental Prediction/National Weather Service/NOAA/*, U.S. Dept. of Commerce, Washington, DC, USA, 2016.

[17] Y. Yung, M. Xue, and G. Zhang, "Simulations of polarimetric radar signatures of a supercell storm using a two-moment bulk microphysics scheme," *J. Appl. Meteorol. Climatol.*, vol. 49, pp. 146–163, Jan. 2010.

[18] C. Augros, O. Caumont, V. Ducrocq, and P. Tabary, "Development and validation of a full polarimetric radar simulator," in *Proc. 36th Conf. Radar Meteorol.*, Sep. 2013, pp. 1–15.

[19] A. Lupidi, S. Lischi, F. Cuccoli, L. Baldini, and N. Roberto, "Validation of the advanced polarimetric Doppler weather radar simulator with Polar55C real observations," in *Proc. 15th Int. Radar Symp. (IRS)*, Jun. 2014, pp. 1–6.

[20] M. Mishchenko, L. D. Travis, and A. A. Lacis, *Scattering, Absorption, and Emission of Light by Small Particles*, 2nd ed. Cambridge, U.K.: Cambridge Univ. Press, 2005.

[21] A. Lupidi, C. Moscardini, F. Berizzi, and M. Martorella, "Simulation of X-band polarimetric weather radar returns based on the weather research and forecast model," in *Proc. IEEE Radar Conf. (RadarConf)*, Kansas City, MO, USA, May 2011, pp. 734–739.

[22] V. N. Bringi and V. Chandrasekar, *Polarimetric Doppler Weather Radar: Principles and Applications*. Cambridge, U.K.: Cambridge Univ. Press, Aug. 2001.

[23] J. A. Milbrandt and M. K. Yau, "A multimoment bulk microphysics parameterization. Part I: Analysis of the role of the spectral shape parameter," *J. Atmos. Sci.*, vol. 62, no. 9, pp. 3051–3064, 2005.

[24] K. V. Beard and C. Chuang, "A new model for the equilibrium shape of raindrops," *J. Appl. Meteorol.*, vol. 44, pp. 1341–1372, Jun. 1987.

[25] P. L. Smith, Jr., C. G. Myers, and H. D. Orville, "Radar reflectivity factor calculations in numerical cloud models using bulk parameterization of precipitation," *J. Appl. Meteorol.*, vol. 14, pp. 1156–1165, Sep. 1975.

[26] M. Tong and M. Xue, "Ensemble Kalman filter assimilation of Doppler radar data with a compressible nonhydrostatic model: OSS experiments," *Monthly Weather Rev.*, vol. 133, no. 7, pp. 1789–1807, Sep. 2004.

[27] G. Zhang, J. Sun, and E. A. Brandes, "Improving parameterization of rain microphysics with disdrometer and radar observations," *J. Atmos. Sci.*, vol. 63, no. 4, pp. 1273–1290, 2006.

[28] J. Sun and N. A. Crook, "Dynamical and microphysical retrieval from Doppler radar observations using a cloud model and its adjoint. Part I: Model development and simulated data experiments," *J. Atmos. Sci.*, vol. 54, pp. 1642–1661, Jun. 1997.

[29] J. S. Marshall and W. Palmer, "The distribution of raindrops with size," *J. Meteorol.*, vol. 5, pp. 165–166, Aug. 1948.

[30] J. M. Straka, D. S. Zrnić, and A. V. Ryzhkov, "Bulk hydrometeor classification and quantification using polarimetric radar data: Synthesis of relations," *J. Appl. Meteorol.*, vol. 39, pp. 1341–1372, Aug. 2000.

[31] V. Ducrocq *et al.*, "HyMeX-SOP1: The field campaign dedicated to heavy precipitation and flash flooding in the northwestern Mediterranean," *Bull. Amer. Meteorol. Soc.*, vol. 95, pp. 1083–1100, Jul. 2014.

[32] R. Ferretti *et al.*, "Overview of the first HyMeX special observation period over Italy: Observations and model results," *Hydrol. Earth Syst. Sci.*, vol. 18, no. 5, pp. 1953–1977, May 2014.

[33] P. C. Waterman, "Matrix formulation of electromagnetic scattering," *Proc. IEEE*, vol. 53, no. 8, pp. 805–812, Aug. 1965.

[34] E. A. Brandes, G. Zhang, and J. Vivekanandan, "Experiments in rainfall estimation with a polarimetric radar in a subtropical environment," *J. Appl. Meteorol.*, vol. 41, pp. 674–685, Jun. 2002.

[35] J. Testud, S. Oury, R. A. Black, P. Amayenc, and X. Dou, "The concept of 'normalized' distribution to describe raindrop spectra: A tool for cloud physics and cloud remote sensing," *J. Appl. Meteorol.*, vol. 40, no. 6, pp. 1118–1140, Jun. 2001.

[36] C. W. Ulbrich and D. Atlas, "Rainfall microphysics and radar properties: Analysis methods for drop size spectra," *J. Appl. Meteorol.*, vol. 37, pp. 912–923, Sep. 1998.

[37] V. Chandrasekar, S. Lim, and E. Gorgucci, "Simulation of X-band rainfall observations from S-band radar data," *J. Atmos. Ocean. Technol.*, vol. 23, pp. 1195–1205, Sep. 2006.

[38] S. Lischi, A. Lupidi, M. Martorella, and F. Berizzi, "X-band full polarized Doppler weather radar return simulation by using propagation-modified ensemble-averaged covariance matrix," in *Proc. 14th Int. Radar Symp. (IRS)*, Jun. 2013, pp. 799–804.

[39] N. Roberto *et al.*, "Test and validation of particle classification based on meteorological model and weather radar simulator," in *Proc. 13th IEEE Eur. Radar Conf. (EuRAD)*, Oct. 2016, pp. 201–204.

[40] A. Battaglia and E. Rustemeier, "PARSIVEL snow observations: A critical assessment," *J. Atmos. Ocean. Technol.*, vol. 27, pp. 333–344, Feb. 2010.

[41] P. Bernabó, F. Cuccoli, L. Baldini, and V. Chandrasekhar, "Super-cooled liquid water droplets detection using dual-polarization radar," in *Proc. IEEE Metrol. Aerosp.*, Jun. 2016, pp. 118–123.

Elisa Barcaroli was born in Florence, Italy, in 1989. She received the B.S. and M.S. degrees *(cum laude)* in telecommunication engineering from the University of Florence, Florence, in 2014, and the Ph.D. degree in information engineering from the University of Pisa, Pisa, Italy, in 2018.

In 2016, she was with Colorado State University, Fort Collins, CO, USA, where she was involved in weather radar polarimetry for her Ph.D. studies. Her research interests include ground-based and avionic weather radars.

Alberto Lupidi received the M.Sc. degree in telecommunication engineering and the Ph.D. degree in remote sensing from the University of Pisa, Pisa, Italy, in 2008 and 2012, respectively.

In 2012, he was with the Delft University of Technology, Delft, The Netherlands, where he was involved in polarimetric weather data processing and polarimetric data decomposition. His research interests include data processing and classification algorithms for radar systems, and signal processing with a particular focus on weather radar polarimetry, SAR, and ISAR polarimetry.

Luca Facheris received the Laurea degree *(cum laude)* in electronic engineering and the Ph.D. degree in information engineering from the University of Florence, Florence, Italy, in 1989 and 1993, respectively.

From 1993 to 2002, he was an Assistant Professor with the Department of Information Engineering, University of Florence, where he has been an Associate Professor since 2002. His research interests include radar and active atmospheric remote sensing and definition of methods for the exploitation of attenuation measurements at microwaves and infrared for the remote sensing of rainfall, pollutants, and tropospheric water vapor.

Fabrizio Cuccoli (M'15) received the Laurea degree *(cum laude)* in electronic engineering from the University of Florence, Florence, Italy, in 1996, and the Ph.D. degree in methods and technologies for environmental monitoring from the University of Basilicata, Potenza, Italy, in 2001.

From 2000 to 2009, he was a Researcher with the Interuniversity National Consortium for Telecommunications (CNIT), Department of Information Engineering, University of Florence. Since 2009, he has been the Head of Research with the CNIT—Radar and Surveillance Systems Laboratory, Pisa, Italy. His research interests include remote sensing of rainfall, water vapor, and atmospheric gaseous components through active systems.

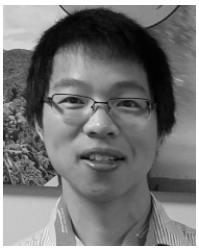

Haonan Chen received the bachelor's degree in electrical engineering from the Chongqing University of Posts and Telecommunications, Chongqing, China, in 2010, and the M.S. and Ph.D. degrees in electrical engineering from Colorado State University (CSU), Fort Collins, CO, USA, in 2013 and 2017, respectively.

He is currently a National Research Council Research Associate with the Physical Sciences Division, NOAA—Earth System Research Laboratory, Boulder, CO, USA and an Affiliate Faculty with CSU. His research interests include radar systems and networking, precipitation classification and estimation with polarimetric radar measurements, multiscale satellite and radar data fusion.

Chandrasekar V. Chandra (S'83–M'87–F'03) received the bachelor's degree in electrical engineering from IIT Kharagpur, Kharagpur, India, in 1981, and the Ph.D. degree in electrical engineering from Colorado State University (CSU), Fort Collins, CO, USA, in 1986.

He is currently a University Distinguished Professor with CSU. He has been actively involved with research and application of weather radar systems. He has co-authored 2 textbooks, 5 general books, and about 200 journal articles.

Dr. Chandra is an Elected Fellow of the International Union of Radio Science (URSI), NOAA/CIRA, and the American Meteorological Society. He served as the Editor-in-Chief for the *Journal of Atmospheric and Oceanic Technology*. He serves as the Chair for Commission F URSI. He was a recipient of numerous awards, including the NASA Technical Contribution Award, the NASA Group Achievement Award, the NASA Robert H. Goddard Exceptional Achievement Award, the Outstanding Advisor Award, the CSU Innovations Award, the IEEE GRSS Education Award, the NOAA/NWS Directors Medal of Excellence, and the Knight of the Government of Finland. He served as the General Chair for the IEEE IGARSS'06 Symposium.